

Constraining the state and evolution of stress within Lucky Strike volcano, Mid-Atlantic Ridge, using a seafloor seismometer network

Michaela Wenner

Abstract

Lucky Strike volcano, located 1700 m beneath the sea surface on the Mid-Atlantic Ridge, hosts one of the world's most active hydrothermal systems. In this study, the orientation of the horizontal components of Ocean Bottom Seismometers deployed in 2008-2009 at the Lucky Strike volcano is measured by P wave and whale song first arrival polarisations. The technique applies a principle component analysis on particle motion ellipses to constrain the difference between the theoretical backazimuth between geographic north and event, and the backazimuth observed by P wave polarisation analysis. After rotation of the seismograms corresponding to the obtained orientation angle, amplitude ratios can be used to better constrain focal mechanisms of earthquakes below the volcano summit. Focal mechanisms obtained show normal faulting between the two northern peaks of the volcano whereas events at the southern peak rupture mostly under compression. An exception is an under extensional stresses rupturing swarm activity following a $ML = 1.6$ event. Making use of the whole data set in following projects can improve the constraints on rupture mechanisms and therefore clarify stress conditions associated with magmatism and cooling below Lucky Strike volcano.

Keywords : ocean bottom seismometer, sensor orientation, submarine volcano, focal mechanisms, hydrothermal circulation

Contents

1	Introduction	3
2	Lucky Strike volcano and data set	3
3	Methodology	5
3.1	Sensor orientation with P wave particle motions	5
3.2	Focal mechanisms	10
4	Results	14
5	Discussion	15
6	Conclusion	19
7	Acknowledgements	19
A	Considerations for OBS orientation	23

1 Introduction

Lucky Strike volcano (LS) is a submarine volcano located at the slow spreading Mid-Atlantic Ridge (MAR) at $37^{\circ}17'$ North. The volcano hosts one of the worlds most active hydrothermal circulation fields with a vent field located at the lava lake in between of three bathymetric highs (Ondréas et al. 1997, Cannat et al. 1999, Humphris et al. 2002, Escartín et al. 2015). At the base of the hydrothermal system an axial magma chamber (AMC) was imaged in 3.0 - 3.8 km depth beneath the volcano (Singh et al. 2006). A seafloor observatory deployed since 2010 gives access to study the surroundings in various scientific disciplines (Thurnherr et al. 2008, Dias et al. 2008, Cuvelier et al. 2009, Martins et al. 2011, Barreyre et al. 2012). A seismic network of five stations deployed around the volcano edifice since 2007 provides an unique data set. The data has thus far been used to study earthquake locations beneath the volcano, indicating event clustering at downflow regions of the hydrothermal circulation (Crawford et al. 2013, Fontaine et al. 2014).

Determining the focal mechanisms of the local earthquakes is the key to understanding the forces acting beneath the volcano. Focal mechanisms describe the source mechanism, therefore the state of stress and the rupture plane of an event. Generally the focal mechanism of an earthquake is obtained by polarity recordings on several seismometers broadly distributed around the epicenter. Making use of the amplitude ratios of compressional and shear waves can improve the resolution of the focal mechanism for local events (Hardebeck & Shearer 2003).

However, raw data recorded at LS volcano are insufficient for determining the focal mechanism as amplitude recordings have to be corrected for sensor orientation. The free-fall OBSs make use of a levelling mechanism to align the Z-component vertically, the horizontal components however are not orientated with respect to geographic north on the seafloor. The measured amplitude of ground displacement on the horizontal components varies with the misorientation of the sensor. For a correct determination of amplitude ratios a corrected instrument orientation is therefore crucial.

This study investigates improving the Lucky Strike observatory seismological data, by determining the geographic orientation of the seismometers horizontal channels for one deployment year (2008-2009). Once orientated, better constrained focal mechanisms of events can be obtained, providing information about the state of stress within the volcano. Using one year of LS data, it is shown that compressional events seem to be centred around the southern peak of the volcano whereas tensional events are located in between the northern peaks. Applying this technique to other years should provide insight on the evolution of stress and the main factors for stress accumulation.

2 Lucky Strike volcano and data set

The study area is situated on the 65 km long Lucky Strike segment, a linear ridge segment of the northern MAR. The segment is characterized by a 10 km wide axial valley and a spreading rate of 20.3 mm/yr (Gripp & Gordon 1990) which places it in the slow-spreading category. Its central volcano is formed by significant along-axis melt supply of the slow spreading ridge with thick crust in the center and ridge-parallel normal faults on both flanks (Escartín et al. 2015). The volcano rises 400m above the seafloor and holds three 100m high peaks on its summit. Between the peaks is a depression with recent lava flows, collapse structures and numerous hydrothermal vents (Ondréas et al. 1997). The volcanic plateau is likely to have emerged during a change in magma supply on the ridge caused by the nearby Azores hotspot (Cannat et al. 1999). Singh et al. (2006) discovered a crustal magma chamber (AMC) approximately 3 km beneath the hydrothermal field of the Lucky Strike volcano.

The data used in this study is part of the MOMAR (MOnitoring the Mid-Atlantic Ridge)

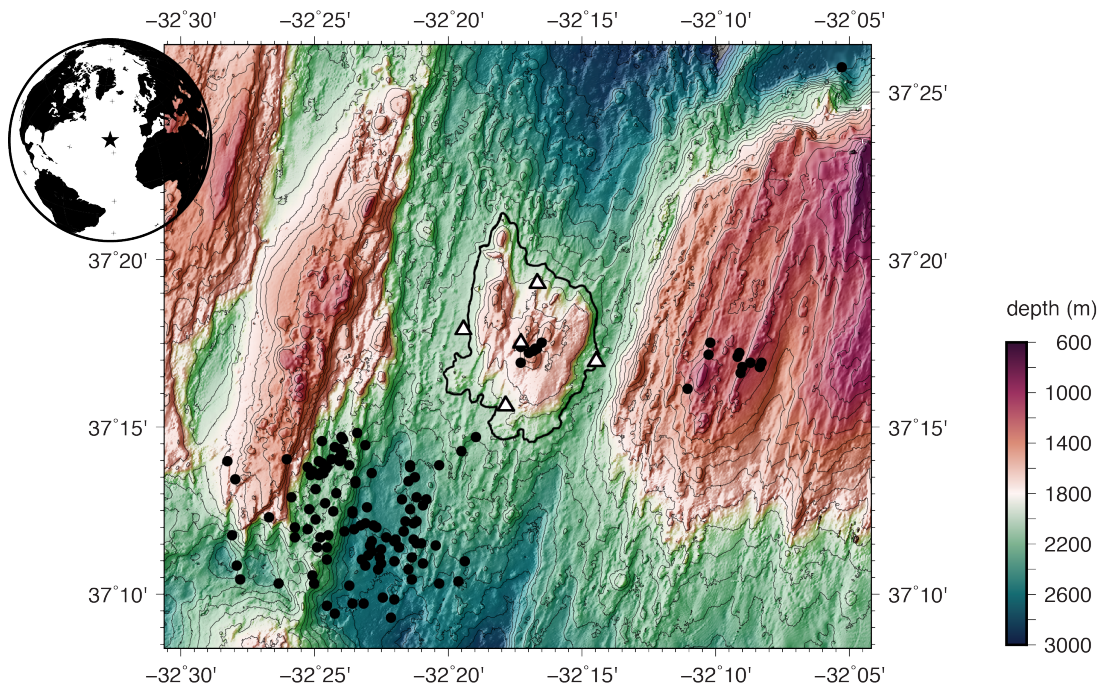


Figure 1 – Bathymetry of Lucky Strike segment with central volcano edifice highlighted by bold contour. The violet triangles mark the position of the five OBSs deployed between August 2008 and August 2009. The black circles represent seismic events during that period with $ML \geq 0.8$. Figure produced with GMT.

project, a multidisciplinary seafloor observatory at the northern MAR. Lucky Strike segment is particularly interesting as a study site, as it hosts one of the most active hydrothermal fields discovered on mid-ocean ridges. This attracts studies in diverse fields of science such as chemistry, biology and geosciences. Its location in the vicinity of the Azores Islands facilitates access to the study area. Various instruments at the LS volcano have obtained data on seismicity, deformation, chemical fluxes, ecology and physical oceanography since 2007 - 2010. (Colaco et al. 2011).

An array of five OBSs has been deployed from 2007 to present day, using yearly deployments from the sea surface. The network focuses on the area around the central edifice to record seismic signals of the active hydrothermal field below the volcano (Figure 1). This ensures almost continuous data coverage over a large time scale. Most of the seismicity within the volcano sits above the AMC at a depth of 1 - 3 km, with two first order clusters of continuous seismicity observed north and south of the summit depression (Crawford et al. 2013). An event swarm was recorded in spring 2009 with event locations deepening by 100 meters below past seismicity.

In this study, data of the deployment period 2008-2009 (stations LSb1, LSb2, LSb3, LSb4 and LSb7) is used. This deployment was chosen because of high data quality and earthquakes that were already well identified and picked. Four of the OBSs used short-period geophones and one contained a broad band seismometer. All instruments used a sampling rate of 62.5 samples per second. Each OBS provides 4 components - orthogonal ground motions and pressure with a frequency bandwidth of 4.5-25 Hz. The lower frequency limit was imposed by the short period geophones and the upper frequency limit by the digital antialiasing filter. The earthquake locations are from Crawford et al. (2013).

For the station orientation measurements a subset of the earthquake catalogue consisting of events with local magnitudes $ML \geq 0.8$ was used. It includes 147 events, with 95 events having $ML \geq 1.0$. The largest event was a magnitude $ML = 3.7$.

3 Methodology

Existing studies on the reorientation of OBSs propose different techniques to obtain the orientation of the horizontal components (Y, X) with respect to geographic north (N,E). Scholz et al. (2017) use P wave and Rayleigh wave particle motions of teleseismic events to orientate the instruments. Zha et al. (2013) determined the orientation with Rayleigh wave polarization retrieved from ambient noise correlation. In the case of the Lucky Strike data however, using teleseismic events is inapplicable due to the limited sensitivity of the geophones to long period energy. The array aperture prohibits the use of surface waves from local seismicity, as they have not yet appeared at the small source receiver distances of this data set. In this study, P wave arrivals of local events within the seismic network are used to determine the orientation angles of the horizontal components of the OBSs. Additionally whale song recordings are used increase the number of measurements and stabilize the results.

3.1 Sensor orientation with P wave particle motions

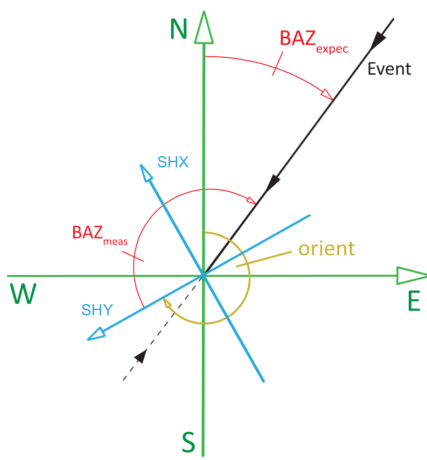


Figure 2 – Principle of orientation of horizontal components with recorded P wave particle motions adapted from Scholz et al. (2017). The green vectors mark geographic north and east, the black vector the direction from the event. The dotted line draws attention to the 180° ambiguity imposed by the P wave polarization measurement while only looking at horizontal particle motions. The blue vectors show the orientation of the two horizontals of the instrument. The angle between the event and geographic north is called BAZ_{expec} , which is the one obtained by looking at event and station location. BAZ_{meas} is the angle obtained through a principle component analysis of horizontal particle motions.

respect to the Y vector (BAZ_{meas}). The difference between BAZ_{expec} and BAZ_{meas} then gives the orientation angle

$$orient = (BAZ_{expec} - BAZ_{meas} + 360^\circ) \bmod 360^\circ \quad (1)$$

where $\bmod 360^\circ$ is the modulo operation (Scholz et al. 2017).

The four components of the deployed instruments record body wave velocities (seismometer/geophones) and pressure waves in the water column (hydrophones). The instrument has a levelling system for the seismometer/geophone, which aligns the vertical component to the gravitational field. The horizontal components are situated at an angle of 90° with respect to one another, but the orientation of these two components with respect to geographic north is unknown.

P waves are, without influences from the subsurface, elliptically polarized in propagation direction. Corresponding particle motions along the ray path can be measured, which gives with a 180° ambiguity, the angle between the miss-oriented horizontal components and the event origin. Figure 2 presents the principle of the applied method, shown graphically. The green vectors mark geographic north and east and the blue vectors mark Y and X components of the OBS. The angle of the wavefront arriving at the station between north and the epicenter of the event is called the backazimuth (BAZ). The expected BAZ (BAZ_{expec}) can therefore be computed knowing the location of station and earthquake. By applying a principle component analysis of the P wave particle motions on the station horizontals, one obtains a BAZ with

To perform the principle component analysis (PCA) of the 3-D elliptical ground motion using the method of Barruol et al. (2006) a Python code based on Fontaine et al. (2009) is used. The covariance matrix, C_{jk} , is calculated

$$C_{jk} = \frac{1}{N_p} Y^T Y \quad (2)$$

with N_p being the number of data points and Y a $N_p \times 3$ centred matrix with Y^T as its transpose. The columns of Y are thereby the east, north and vertical up component, from which their mean has been subtracted. The symmetry of the covariance matrix C_{jk} allows the computation of the eigenvalues and eigenvectors. That way the principle components of the particle motion ellipses are obtained. The apparent horizontal polarization angle θ is calculated as the arctangent of the first two entries of the eigenvector a^1 corresponding to the largest eigenvalue λ^1 .

$$\theta = \arctan \frac{a_2^1}{a_1^1} \quad (3)$$

This procedure is done twice in 2-D (horizontal components and longitudinal and vertical components) and once in 3-D to obtain the apparent BAZ. The longitudinal component L thereby being $L = \cos(\theta + \pi)N + \sin(\theta + \pi)E$, with N and E being the horizontal components. The vertical particle motion, derived from the vertical and longitudinal component, gives the incidence angle to resolve the 180° ambiguity. The error of the apparent incidence angle ER_INC_{app} is given by

$$ER_INC_{app} = \tan^{-1} \sqrt{\frac{\beta_2}{\beta_1}} \times \frac{180^\circ}{\pi} \quad (4)$$

where $\beta_1 \geq \beta_2$ are the ordered eigenvalues of the covariance matrix of the vertical and longitudinal component. A control parameter of the accuracy of the measurement is given by the rectilinearity (CpZ for the vertical and CpH for the horizontal). Rectilinearity is a measure of ellipticity of the analysed data cloud. The closer the rectilinearity is to one, the more linear its shape and the more accurate the measurement in principal. CpZ is defined as:

$$CpZ = 1 - \frac{\beta_2}{\beta_1} \quad (5)$$

For CpH the eigenvalues of the covariance matrix of the horizontal components are used (Scholz et al. 2017).

The error of the P wave polarization measurement is calculated as Fontaine et al. (2009):

$$ER_BAZ_{meas} = \sqrt{\frac{1}{N} \sum_{i=1}^M (x_i - \bar{x})^2} \quad (6)$$

To calculate the averaged station orientations from several estimates, a weighted mean over all measurements in the chosen measurement window was calculated. The weights were applied according to measurement error, SNR and rectilinearity of the measurement. To estimate the error the circular mean error is calculated by

$$ER_{circ_mean} = 2 \sqrt{2(1 - R)} \times \frac{180^\circ}{\pi} \quad (7)$$

with

$$R = \frac{1}{N} \sqrt{\left(\sum_{i=1}^N \cos orient_i \right)^2 + \left(\sum_{i=1}^N \sin orient_i \right)^2} \quad (8)$$

being the mean resultant length of the circular distribution (Scholz et al. 2017).

To ensure the accuracy of the algorithm, the program was tested using arrivals of several distant earthquakes at a seismic land station (FUR, Germany), for which the location of the earthquake and station as well as the sensor orientation are known. The measurement of the P wave particle motion and the BAZ should then give the same angle. The tests performed well (within a few degrees) for events distributed broadly around the station.

A threshold of 0.7 for rectilinearity was set and P wave polarisation measurement were performed for earthquakes with a magnitude $ML \geq 0.8$ due to less ambiguity of P wave onsets. A higher rectilinearity threshold would have reduced the allowed events and therefore important information. Earthquake locations were taken from the earthquake catalogue of Crawford et al. (2013). Events outside the array were discarded due to large localization errors. The data was preprocessed using the ObsPy software suite (Krischer et al. 2015). Mean and trend were removed from the data and it was tapered with a Hanning window. After several computations with different parameters to minimize measurement errors, the frequency band was set to 6-12 Hz and the window length was set to 0.3 s. The lower corner frequency of the bandpass filter is imposed by the short period instruments. With lower frequencies, the sensitivity of the geophones decreases rapidly. All measurements were checked visually to ensure that they were not influenced by noise or different signals on any component. Figure 3 shows a P wave polarisation measurement of a $ML = 1.3$ event in late August, 2008. The waveform has been filtered according to the determined values and the analysis was done on a window of 0.3 s after the P wave arrival time. The PCA on the horizontal components constrains the BAZ of the instrument with respect to the event (BAZ_{meas}). The vertical versus longitudinal particle motion resolves the 180° ambiguity. The signal to noise ratio (SNR) of 19.6, horizontal rectilinearity of 0.95 and 2-D particle motion error of 12.42° are within acceptable boundaries. The accepted value of maximum measurement error is 20° . BAZ_{meas} is estimated to 119° whereas the expected BAZ is 24° . For this event, equation 1 gives an orientation angle of 262° for the horizontal components of station LSb7 with respect to geographic north.

In this study sub-sensor anisotropy is not taken into account. Seismic anisotropies can influence, albeit only on the last wavelength beneath the receiver, the P wave polarization direction by $\geq 10^\circ$ (Fontaine et al. 2009, Schulte-Pelkum et al. 2001). As measurements on the the BAZ calculated with P Wave particle motions of events recorded at the OBSs around the LS volcano have errors $> 10^\circ$, anisotropy should not impair the results excessively.

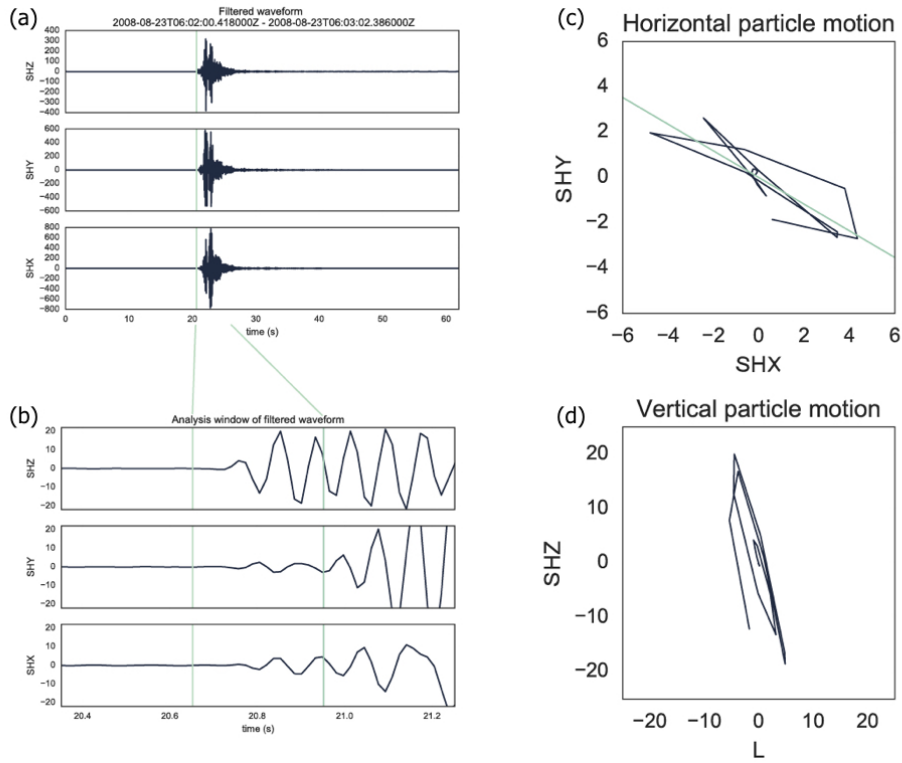


Figure 3 – P wave polarization measurement of a local event of $ML = 1.3$ in August, 2008 recorded on station LSb7. (a) Filtered waveform of the event on component SHZ, SHY and SHX, the vertical line is marking the P wave arrival, (b) zoom on P wave arrival. Vertical lines define the measurement window, (c) horizontal and (d) vertical particle motions to estimate BAZ.

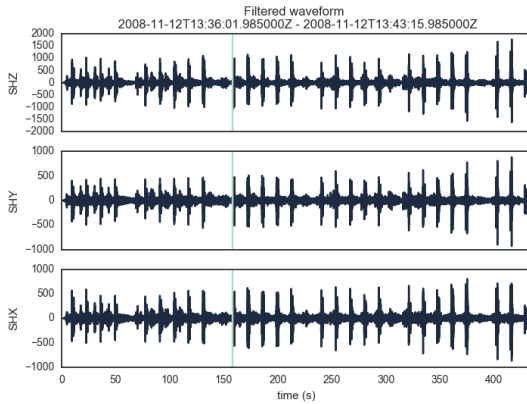


Figure 4 – Seismogram of fin whale songs recorded at station LSb7 on channel SHZ, SHY and SHX. The data has been filtered between 10 - 28 Hz. The green line marks the first arrival of the selected whale call. The x axis describes the time in seconds, the y axis the amplitude of the signal.

of these signals can be found on OBS data, even if whales are not always in the vicinity of the network. Despite whale location being obtained through simplified models, the measurements agree with the P wave first arrival measurements of local earthquakes. Hence, whale songs can increase the number of measurements drastically and improve the constraint on the orientation angle.

To confirm the results obtained, measurements were also performed on whale song data. The frequency range of fin whale songs lies exactly in the frequency band recorded by the geophones. With a simplified velocity profile for the water column and a continuous sound velocity of 1.5 km/s, satisfactory whale locations could be obtained. Large anisotropies in the water column can be excluded and the sharp arrivals of the signal suggest that the measurements are fairly accurate. The advantage of measurements being performed on whale song data is the frequency of occurrence and the non-interference with subsurface anisotropies. In Figure 4 filtered waveforms of whale song recordings are shown. Each amplitude peak corresponds to a different whale song. The timescale being only 400 s shows how many

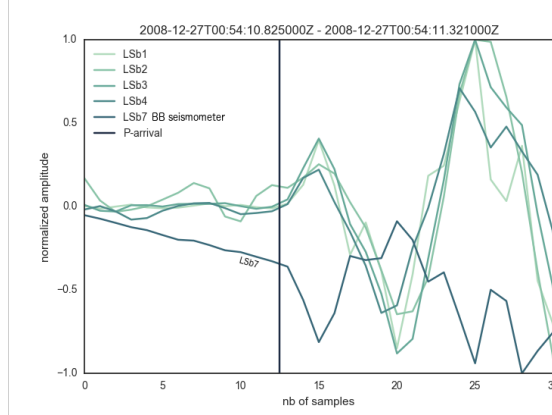


Figure 5 – Comparision of P wave first arrival polarities on Stations LSb1, LSb2, LSb3, LSb4 and LSb7. The dark vertical line marks the P wave first arrival. Shown are the 30 samples on every station which corresponds to roughly half a second.

an earthquake is shown. The event, being a regional earthquake on the Z component on all five stations. One can see that Station LSb1 to LSb4 (geophones) are inverse polarized with respect to station LSb7 (BB seismometer).

P wave particle motion measurements were performed on stations LSb1, LSb2, LSb3, LSb4 and LSb7. Depending on the data quality of the individual stations, two to four events were selected to give accurate measurements. To confirm the results measurements were also made with whale songs recorded by the seismometers. Combining the two, measurement windows were defined for each station. In these, measurements were taken into account to obtain a mean orientation angle.. Without deciding for one set of measurements, the 180° ambiguous measurements would severely distort the results. Choosing the wrong angle with 180° difference to the actual orientation angle should not influence the accuracy of the focal mechanisms. In Figure 6 the seismogram of the Y component and the seismogram of the to north rotated Y component, are shown. A difference in amplitude is clearly visible and affects the accuracy of amplitude ratios for focal mechanism computation. The third seismogram was rotated with a difference in angle of 180° to the angle the second was rotated with. The waveform is now reverse polarized, but the absolute amplitude has not changed. The measurements for all stations are listed in Table 1. LSb7 gives the best constrained orientation angle with the most measurements compared to the other stations and has no 180° ambiguity. However, on station LSb1, LSb2 and LSb4, the ambiguity is very pronounced (Figure 7). Station LSb3 gives the orientation angle with the largest scatter, therefore the highest uncertainty,

To obtain the correct P wave polarity measurements, it is crucial to know the design of the instruments used for recording. Following SEG (Society of Exploration Geophysics) standard, the four deployed geophones are polarized in accordance with a right handed coordinate system. Z being positive downwards, and Y being in a 90 degree angle clockwise to X (Brown et al. 2000). For seismological recordings, a left handed coordinate system (GSN standard) is used with Z positive upwards, as is the case for the deployed broad band seismometer. This leads to a reversed polarity in the recordings of the geophones (Figure 5). Consequently, to obtain correct particle motion measurements one has to reverse the polarities of the geophone Z components. In Figure 5 the P wave first arrival of

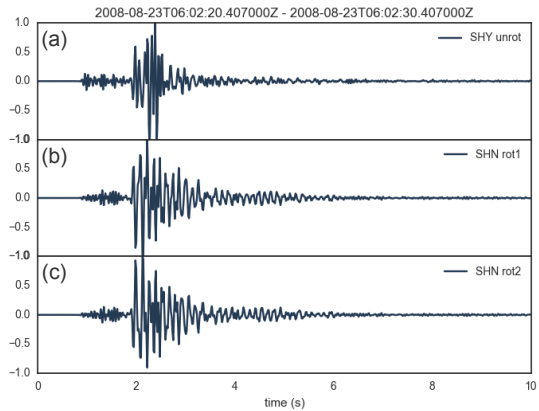


Figure 6 – Comparison of waveforms of (a) the raw recording, (b) a rotated recording with rotation angle 1 (rot1), and (c) another rotation angle (rot2), 180° different to rot1. The amplitude difference between (a) to (b) and (c) is well pronounced. The amplitudes for (b) and (c) are equal but an inverse polarity can be observed. The x axis shows the time in seconds and the y axis the normalized amplitudes of the recordings.

is now reverse polarized, but the absolute amplitude has not changed. The measurements for all stations are listed in Table 1. LSb7 gives the best constrained orientation angle with the most measurements compared to the other stations and has no 180° ambiguity. However, on station LSb1, LSb2 and LSb4, the ambiguity is very pronounced (Figure 7). Station LSb3 gives the orientation angle with the largest scatter, therefore the highest uncertainty,

Station	Nb of EQ	Nb of WS	Nb of events in window	orientation	error
LSb1	3	3	3	69°	16.77°
LSb2	2	2	2	164°	17.62°
LSb3	4	6	5	62°	42.50°
LSb4	2	1	2	253°	3.27°
LSb7	4	3	7	257°	7.97°

Table 1 – P wave polarisation measurements for all 5 stations. Listed are station name, the number of earthquakes and number of whale songs chosen to give accurate measurements, the number of events that were used for the orientation calculation and orientation angle and its error.

Orientation angles on all five stations are shown in Figure 7. The angles are plotted against the magnitude of the event on the r axis of the polar plot. The color code corresponds to the measurement errors. Events plotted on the outer circle are whale song measurements. For representative reasons, they were assigned a magnitude of 4, to separate them from earthquake measurements. Measurements of events whose epicenter is not located within the array had to be excluded from the results. The uncertainty of the earthquake localisation is very high and often the error ellipse spans over the whole network (Figure 8). BAZ_{meas} can thus be accurately estimated but BAZ_{expec} cannot.

3.2 Focal mechanisms

To describe mechanisms of seismic sources the concept of a double couple point source has been introduced. A double couple of forces acts on a rigid body and ruptures on a fault plane with an auxiliary plane perpendicular to it. In the quadrants defined by these planes, there is either compression, which correlates with an upward first motion on the recorded seismogram or dilatation, which correlates with a downward first motion (Brown et al. 2000). Waveforms recorded on an array of instruments distributed around a hypocenter can therefore constrain the stress state (tensional or compressional) of the surrounding rocks. In the case of the LS volcano however, the limited station coverage leads to a large non uniqueness of the solutions for the focal mechanism, when only picking polarities. Studies have shown that the usage of S/P Amplitude ratios can improve the constraint of fault plane solutions for small local earthquakes (Kisslinger 1980, Hardebeck & Shearer 2003).

The displacement field of a seismic point source can be written as a convolution of the moment tensor and the gradient of the Green's function, a third-order tensor field $u_n = M_{pq} * G_{np,q}$ (Aki & Richards 2002). The Green's function defines the impulse response of the medium the wave is propagating through. The moment tensor is a first order approximation of the forces of a seismic point source (Jost & Herrmann 1989). The equivalent forces form a double couple which defines the forces on the fault plane and an auxiliary plane perpendicular to it. The displacement field of a double couple point source is described as

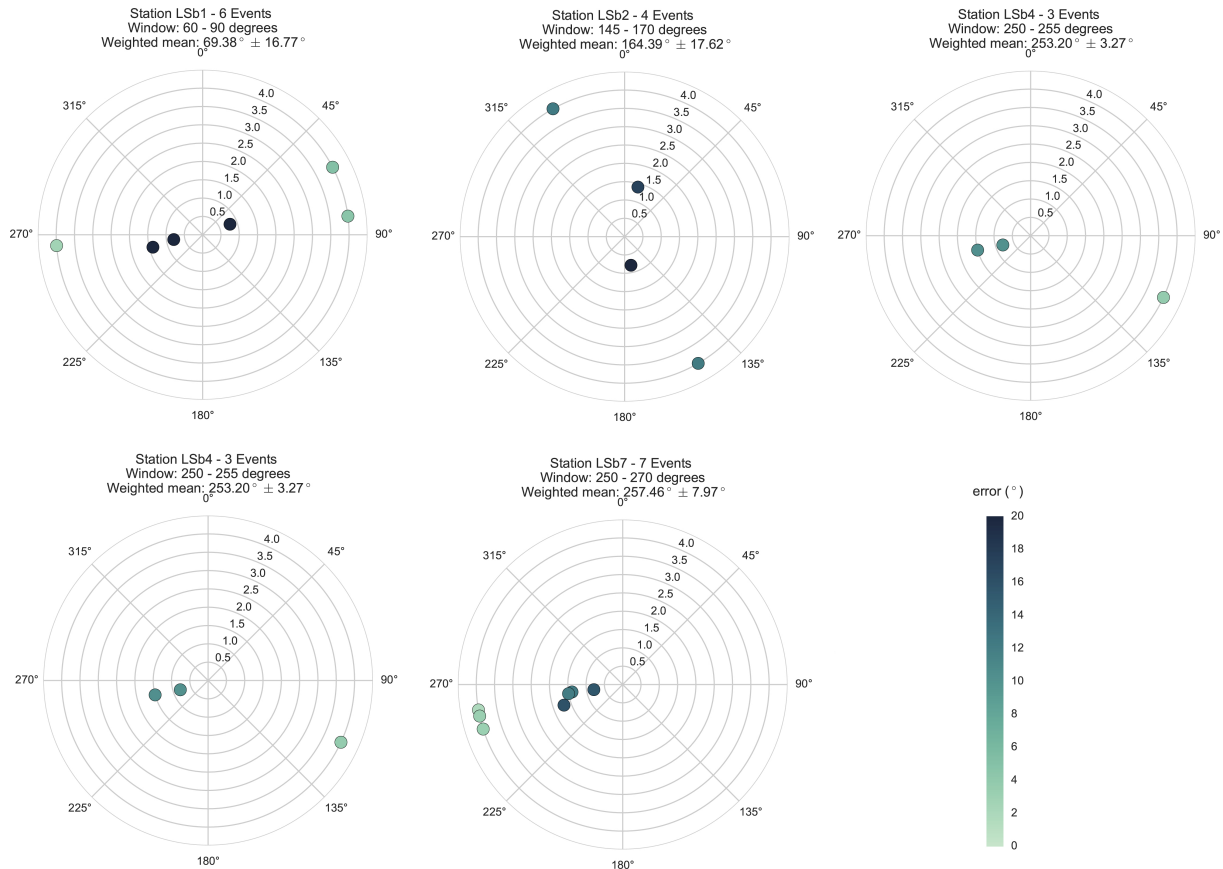


Figure 7 – Orientation results for all stations. The angle gives the orientation of the instruments with respect to geographic north. The radius gives the magnitude of the events. All measurement points plotted on magnitude 4.0 are P wave polarization measurements of whale songs, which do not have a magnitude. The color code refers to the error of the P wave polarization measurement.

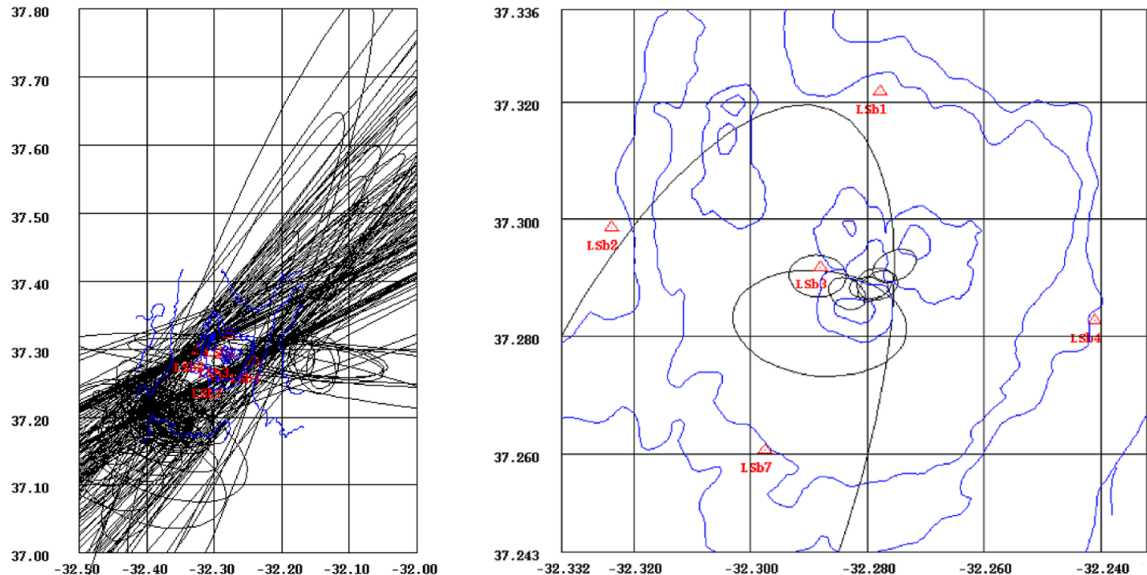


Figure 8 – Map and zoom in on error ellipses of events (black), stations (red) and major geological features at LS volcano (blue) plotted in SEISAN software suite (Havskov & Ottemöller 2008).

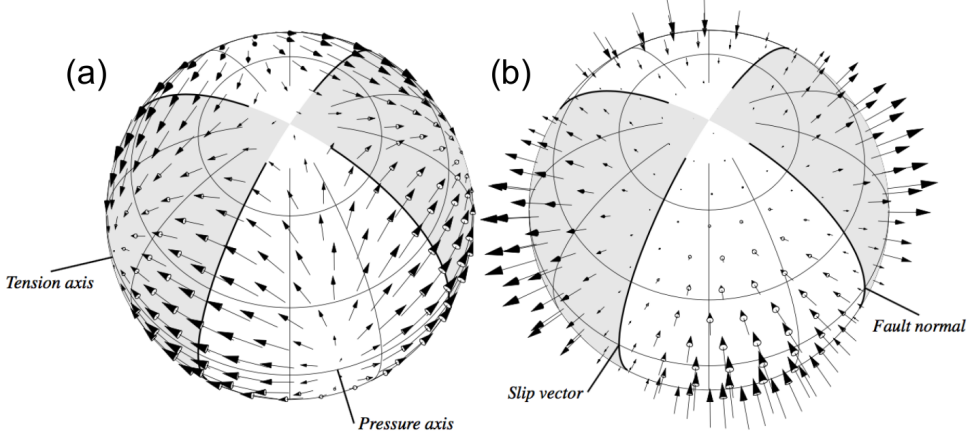


Figure 9 – Illustration of the displacement pattern of a double couple source with shear dislocation and fault and auxiliary plane after Shearer (2009). The darker areas represent compression corresponding to an upward movement of the P wave first arrival, whereas the lighter areas represent dilatation corresponding to a downward movement of the P wave first arrival. The vectors illustrate the amplitudes of the first arrivals of (a) S waves and (b) P waves. One can clearly see that amplitudes are larger for S waves next to the planes and for P waves at the pressure/tension axis.

$$u(x, t) = \frac{1}{4\pi\rho} A^N \frac{1}{r^4} \int_{\frac{r}{\alpha}}^{\frac{r}{\beta}} \tau M_0(t - \tau) d\tau \quad (9)$$

$$+ \frac{1}{4\pi\rho\alpha^2} A^{IP} \frac{1}{r^2} M_0\left(t - \frac{r}{\alpha}\right) + \frac{1}{4\pi\rho\beta^2} A^{IS} \frac{1}{r^2} M_0\left(t - \frac{r}{\beta}\right) \quad (10)$$

$$+ \frac{1}{4\pi\rho\alpha^3} A^{FP} \frac{1}{r^2} \dot{M}_0\left(t - \frac{r}{\alpha}\right) + \frac{1}{4\pi\rho\beta^3} A^{FS} \frac{1}{r^2} \dot{M}_0\left(t - \frac{r}{\beta}\right). \quad (11)$$

with ρ being the density of the material, α and β the P and S wave speeds, respectively, A the radiation patterns and $M_0(t)$ the time-dependent seismic moment (Aki & Richards 2002). The Green's function accounts then for properties in the radiation of the waves, whereas the seismic moment describes characteristics of the source processes. The three terms represent the near-field (9), intermediate-field P and S displacement (10) and the far-field P and S displacement (11). A is thereby the radiation pattern. The radiation patterns for near, intermediate and far-field are all proportional to the radial component:

$$R = \sin 2\Theta \cos \Phi \hat{r}, \quad (12)$$

and the transverse component

$$T = \cos 2\Theta \cos \Phi \hat{\Theta} - \cos \Theta \sin \Phi \hat{\Phi} \quad (13)$$

The displacement field set up by a double couple force (shear dislocation) can therefore be described by only these two radiation patterns (Aki & Richards 2002). In Figure 9 the quadrant distribution of the displacement of S waves (a) and P waves (b) caused by a double couple source is shown. The shaded quadrants describe areas of compression whereas the light areas describe dilatation. The vectors represent the amplitude of the displacement.

The fault plane solution is defined by three angles: strike, dip and rake. Strike is the azimuth of the fault plane, dip is the clockwise measured angle from the horizontal to the hanging wall and

rake is the slip direction measured on the fault plane (Snoke 2003). The planes are plotted on a focal sphere with the source in the center which is in turn projected on the lower half of a focal sphere (Aki & Richards 2002). By picking the polarity of the first arrivals at various stations, one can define the orientation of the fault and auxiliary plane. The amplitude ratios are assumed to evolve systematically because of the behaviour of amplitudes near the nodal planes. P waves have smaller amplitudes near the planes and are largest near the pressure (P) and tension (T) axis, whereas S wave amplitudes behave in a reversed manner (Figure 9). Since amplitude ratios are used, it is not necessary to take geometrical spreading and the magnitude of the event into account, but only differences in P and S wave attenuation (Hardebeck & Shearer 2003).

The computation of the focal mechanism has been performed and compared with two different programs distributed in SEISAN software suite (Havskov & Ottemöller 2008). The program FOCMEC (Snoke 2003) performs a grid search on the whole sphere and gives several possible solutions as an output. From amplitude readings of P-phase and S-phase, SV on Z component and SH on the transverse component, it computes SV/P, SH/P and SV/SV ratios. All possible solutions within the defined limits: the number of polarity errors, ratio errors, root-mean square errors for the ratios used, and for all ratios, are listed as output. The user can then decide which solution fits best. The program HASH (Hardebeck & Shearer 2002, 2003) uses the same amplitude ratios and polarities as FOCMEC to constrain the focal mechanism. The parameters to define in HASH are the number of polarity errors and a limit for average amplitude errors. The difference from FOCMEC is that if no solutions are found, the program increases its limits to find the best fitting fault plane solution. HASH then returns one or a few best solutions. The advantage is that the user does not have to decide which of the many different solutions fits best. The program calculates errors of the plane orientation and average amplitude errors (Havskov & Ottemöller 2008).

In order to better estimate the influence of amplitude picking on focal mechanisms of events recorded in a setting similar to LS volcano, a quantitative evaluation with synthetic seismograms was performed. The program Axitra (Coutant 1989) was used to generate synthetic seismograms. The test was performed using two different focal mechanisms and two different hypocenters within the MOMAR array. The seismic moment was set to $M_0 = 7.5e12Nm$ ($M_w = 2.55$), a step source time function was chosen with a duration of 0.05 s and the output was set to velocity to conform with seismometer recordings. The tests showed that five polarity recordings can give an accurate estimate of the focal mechanisms if the amplitude ratios are taken into account. Figure 10 shows the result of the measurements done on synthetic waveforms of an event with normal faulting. The receiver locations correspond to the locations of LS volcano. The 1D velocity model beneath LS volcano was used (Crawford et al. 2013). The filtering and amplitude picking was performed following Hardebeck & Shearer (2003). The data was bandpass filtered between 1 - 15 Hz. The P wave amplitude was picked at the peak of the first half-cycle of the direct arrival and the S wave amplitude was picked as the maximum amplitude within two seconds after the S wave arrival. The original solution to generate the synthetics was set with a strike = 0° , dip = 45° and rake = -90° . With HASH, and without taking the amplitude ratios into account, a fault plane solution with strike = 24° , dip = 24° and rake = -114° was obtained. By adding the amplitude ratios to the measurements the result could be improved to strike = 12° , dip = 51° and rake = -71° when using the FOCMEC program. One can see that the amplitude ratios improve the result of the measurements. The best solution was obtained by picking the solution with the smallest RMS error of the FOCMEC program. The amplitude ratios distort the HASH measurements to a fault plane solution with strike = 22° , dip = 73° and rake = 110° for this geometric setting. Adding more stations around the event improves the solution when only taking the polarities into account. However, by adding the amplitude ratios the errors become larger, and thus a larger number of stations has a negative influence on the accuracy of the fault plane solution. Similar results were obtained for a second

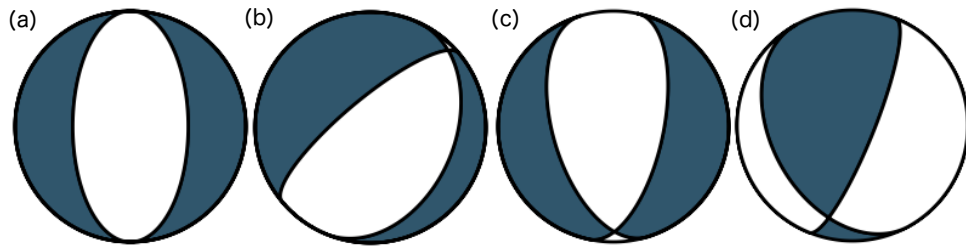


Figure 10 – Focal mechanisms obtained from synthetic seismograms on five receivers corresponding to the LS volcano station locations, using first arrival directions and amplitude ratios in HASH and FOCMEC. The input to generate the seismogram was a normal fault focal mechanism with strike = 0° , dip = 45° and rake = -90° . (a) true focal mechanism, (b) HASH without amplitude ratios, (c) FOCMEC with amplitude ratios and (d) HASH with amplitude ratios.

test with a focal mechanism of strike = 220° , dip = 50° and rake = 80° and an event location less centred than the previous one.

4 Results

Orientation corrected seismograms allow the usage of amplitude ratios to constrain focal mechanisms and therefore the stress regimes in the subsurface. After obtaining the best possible orientation angles, the Y and X components of the recordings were rotated with ObsPy to N and E components according to the obtained orientation angles. Polarities and amplitudes were then picked for 15 Events with epicenters within the network with $ML \geq 0.1$ and clear P arrivals. The polarity of the P wave first arrivals are clearly readable for every station. An error within polarity readings is therefore improbable. The amplitudes were not measured on stations LSb2 and LSb3, as the error of the orientations is especially large on these stations and thus the rotation and amplitudes are not reliable.

The programs HASH and FOCMEC were used to obtain the best fitting focal mechanism. FOCMEC solutions were chosen to be the most accurate ones. HASH, searching for the best possible results expands the limits given and assumes in most cases one wrong polarity reading. Amplitude measurement errors however, are essentially more probable due to rotation errors of the seismogram. With FOCMEC, the solutions with the five correct polarity readings, the least incorrect amplitude ratios and the smallest error on the amplitude ratios and overall error was found.

The results of the FOCMEC computations are presented in Figure 11(a). The focal mechanisms are scaled corresponding to the magnitudes. The biggest magnitude is $ML = 1.6$ and the smallest $ML = 0.1$. Figure 11(b) shows the focal mechanisms plotted as a function of depth over time. The number of events considered each month depends on the clarity of the polarisations on each station and the magnitude of the events. A high number of events is observed in spring 2009, during a seismic swarm. There are two main types of focal mechanisms present in this data set. Reverse faulting is characterised by a strike of $14 \pm 7^\circ$, a dip of $54 \pm 18^\circ$ and a rake of $69 \pm 10^\circ$, with 8 events of similar geometry taken into account. Considering 4 events of normal faulting, strike, dip and rake are defined by $250 \pm 8^\circ$, $30 \pm 10^\circ$ and $-34 \pm 13^\circ$. Three other events of normal fault type with different strike angles are not taken into account.

Compressional stresses are thereby mostly present around the southern peak, while the northern peak seems to be dominated by tensional stresses. The three events with normal faulting in spring 2009 around the southern peak can be associated with swarm activity. Even though the uncertainty of the focal mechanisms obtained in this study might be high in terms of fault

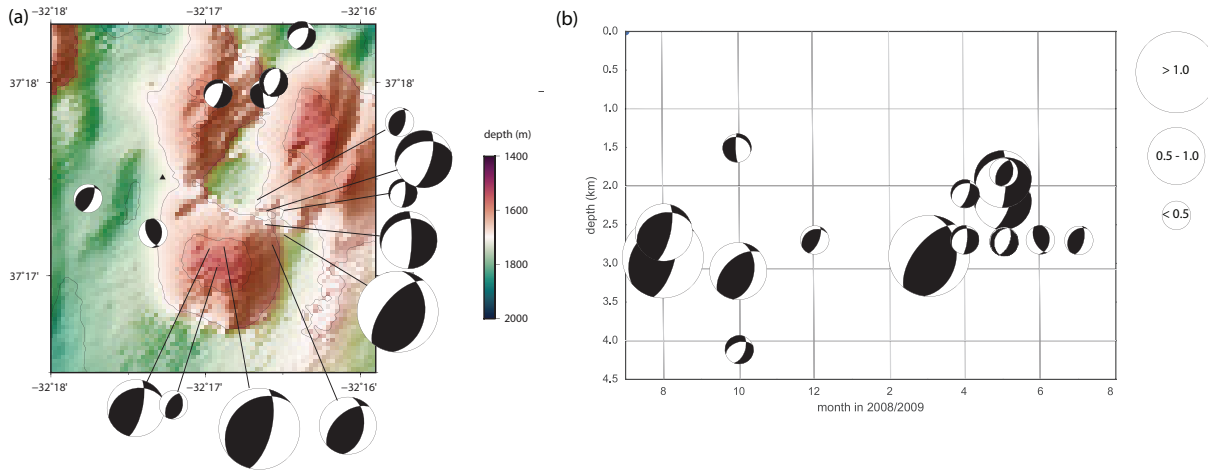


Figure 11 – (a) Focal mechanisms of 15 events on LS volcano over the year 2008/2009 with $ML \geq 0.1$. The focal mechanisms are scaled corresponding to the event magnitudes: The smallest focal mechanisms represent events with $ML < 0.5$, intermediate represents $ML \leq 1$, and biggest represent events with $ML > 1$. Colorcode marks depth below sealevel (b) Beach balls plotted as a function of depth (km) against time (month in 2008/2009). The size is again proportional to the event magnitude. Y axis marks the depth below the seafloor.

plane orientations due to wrong amplitude picking or wrong orientation angle of the sensors, the first motion of the P wave arrivals is very distinct. The central station LSb3 clearly suggest compressional mechanisms for most events at the southern peak and the flanks of the southern peak.

5 Discussion

The quality of OBS orientation measurements with P wave first arrival particle motion at Lucky Strike volcano vary largely between the different stations. To obtain an accurate result for the particle motion measurements, it is crucial to pick the exact P wave arrival for every event. A high noise level on one or more components can also affect the measurements. Particle motions will then be dominated by the direction of the noise, instead of the P wave first arrival. Another drawback of the LS data set are the earthquake localisation errors. As shown in Figure 8, localisation errors for events outside the array can span the whole network. Consequently, a comparison of BAZ obtained by the P wave particle motion and the earthquake location is inconclusive. It is therefore important to determine thresholds for parameters like SNR, earthquake localisation errors and rectilinearity of the particle motion ellipses to ensure accurate measurements.

Theoretically the P wave particle motion measurements can constrain the 180° ambiguity when taking the incidence angle of the wavefront into account. However, the incidence angle of the events is very steep. With measurement errors this can then lead to a wrong classification of the vertical particle motion. Figure 7 shows clearly that the 180° ambiguity is not perfectly resolved for most of the stations. When choosing the angle for the orientation which would have been obtained by taking the ambiguous measurements instead of the window chosen now, the seismogram would be reversed. This means taking an angle which is different by about 180° will reverse the polarity of the horizontal recordings but the amplitudes will not change. As the P wave polarity is only measured on the Z component which is not influenced by the rotation of the seismograms, a 180° mistakenly chosen angle should not influence the focal mechanisms. The incidence angle of the events is likely also the reason for the scattered measurements on

station LSb3. This station is located in the summit depression and therefore very close to the epicenters of the events. The small distance leads to weak horizontal particle motion recorded by the seismometer which falsify the measurements and lead to the large variety of obtained orientation angles as observed at station LSb3.

Another source of errors in P wave particle motion measurements are seismic anisotropies. Strong anisotropies caused by lattice-preferred orientation of olivine crystals and the presence of melt bodies and cracks in the subsurface have been proposed and modelled for mid-ocean ridges (Hess 1964, Blackman & Kendall 1997, Nowacki 2013). Regarding the frequency band examined in this study and restricted sensitivity of P wave to one wavelength, P wave polarization is influenced by anisotropies from about 1 km beneath the instrument. Fontaine et al. (2009) utilized a harmonic analysis to estimate the influence of seismic anisotropy in P wave polarization. This allows a distinction of the effects on the particle motion angle. Effects of anisotropy are thought to be rather small (Crampin et al. 1982) but to minimize errors should be considered.

The obtained focal mechanisms give insight on the stress distribution in the crust below the LS volcano. Past studies of microseismicity above the axial magma chambers at spreading ridges found that fracturing due to hydrothermal circulation imposes significantly more stress on surrounding rocks than do tectonic stresses (Sohn et al. 1999, 2004, Wilcock et al. 2002, 2009, Lowell & Germanovich 1994). There are several different theories explaining resulting seismicity:

(1) Sohn et al. (1999) link normal faulting events with contraction of the underlying AMC due to hydrothermal cooling. They observe a close relationship between temperature change in the hydrothermal system and microseismicity at the fast spreading East Pacific Rise. Based on the vertical seismic pattern, tectonism as trigger is improbable. The earthquakes are located within the hydrothermal system which suggests thermal strain due to cooling and therefore contraction at the AMC as a trigger for microseismicity. Tensional stresses are increased by the subsidence of the AMC roof until vertical existing cracks and faults fail under the stress. They argue that events can not exceed a certain magnitude because tectonic tensile stresses are continuously released at the base of the hydrothermal system by thermally induced microearthquakes,

(2) Sohn et al. (2004) propose thermal contraction at the base of the hydrothermal circulation cells as the source of events, based on the seismicity pattern after an eruption at the Axial Volcano, Juan de Fuca Ridge. After the eruption, seismicity decreased slowly over the following two months, which they linked with magma intrusions that draw near the surface. At the dike walls, one gets thereby compressional stresses which compensate tensile stresses due to tectonic processes during rifting. At the peak of the dyke one observes mechanical stresses which are thought to cause normal faulting events at the Axial Volcano. Additionally, the cooling of the intruded lava and pressure changes at the AMC are thought to enhance microcracking,

(3) Wilcock et al. (2009) associate observed seismic pattern with stress induced by a pressurized magma chamber. They rule out the possibility of extensive seismicity triggered by hydrothermal cooling because of the along axis alignment of the fault planes strikes. Instead, they postulate the theory that inflation/deflation of the AMC is the trigger for seismicity at hydrothermal fields. In their model, they consider an AMC with two towards-one-another dipping normal faults, cutting from the surface to the edges of the AMC. During the inflation, tensional stresses are generated directly above the AMC due to an injection of material in the rock body. Compressional stresses are generated on both sides of the injected body, thus on the flanks of the inflated AMC. This is consistent with the observations at the Endeavour segment of the Juan de Fuca ridge.

None of the above theories seems to fit the observations at LS volcano. Subsidence of the AMC

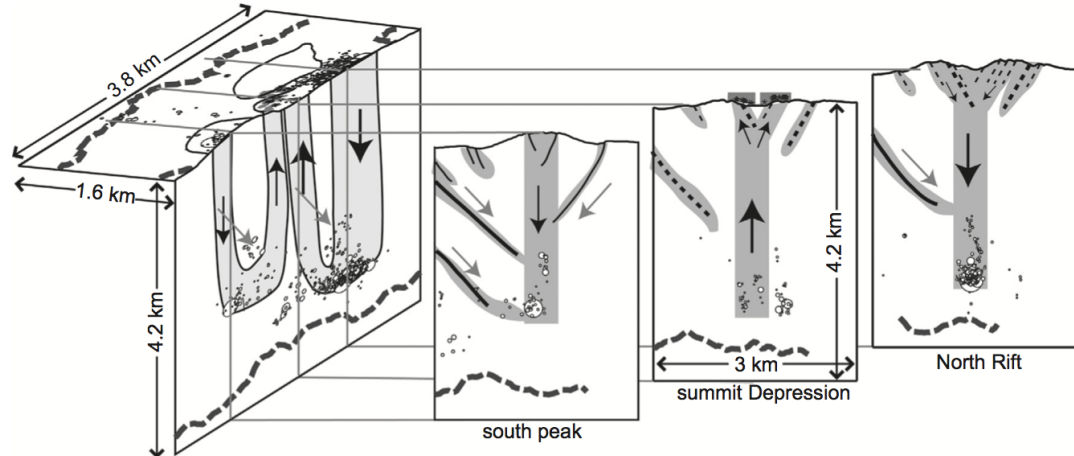


Figure 12 – Hydrothermal circulation at LS volcano proposed by Crawford et al. (2013). Microseismicity is located at the base of the hydrothermal system.

roof due to cooling and thus contraction, as proposed by Sohn et al. (1999), is supported by the axis alignment of the normal faulting mechanisms and the location on the edges of the AMC, but do not explain the compressional mechanisms observed at the southern peak of LS volcano. The seismicity pattern observed by Wilcock et al. (2009) is not seen at LS and the lack of vertical displacement which should be observed considering an inflation of the AMC does also not support their preferred model (Crawford et al. 2013). Nevertheless the temporal pattern of the seismicity below the southern peak could be explained by a combination of above mentioned theories. A small magma injection in the rock body directly above the AMC could lead to compressional stress directly above the magma chamber. The cooling and therefore contraction of the injection could then explain the swarm activity after the magnitude 1.6 event in march 2009 (Sohn et al. 2004).

Crawford et al. (2013) studied the seismicity at the LS volcano and linked the spatial pattern of the events to a thermal strain on the base of the hydrothermal circulations cells as proposed by Sohn et al. (2004) . The concentration of epicenters near the northern two peaks and the southern peak suggests cooling induced cracking triggered by the downflow of cool fluids. Their proposed model for the hydrothermal circulation therefore suggests downflow on the northern and southern peak of LS volcano and upflow in the center (Figure 12). The prefered model correlates with numerical simulations by Fontaine et al. (2014) in which the 3-D flow architecture of the hydrothermal flow at LS volcano is examined. Considering this, a tensional stress regime is expected at both downflow regions due to thermal strain (Lister 1974). The dominance of compressional mechanisms on the southern peak is in conflict with this assumption. Cooling induced stresses on surrounding rocks induce tensile regimes, whereas heating induced cracking induces in compressional regimes (Browning et al. 2016). Tensile regimes should thereby be more numerous, which has been shown by experiments on thermally stressed volcanic rocks (Browning et al. 2016). The number of events recorded on the southern peak is significantly smaller than between the northern peaks (Crawford et al. 2013). This suggests that there may be upflow below the southern peak of the LS volcano. Numerical models on the influence of seafloor bathymetry on the vent field, specifically for the LS volcano, suggest a deviation of the upflowing plume towards the bathymetric high (Bani-Hassan et al. 2012). According to this model the upwelling would be focused and stabilized below the southern peak of the volcanic edifice. Topography of the AMC roof is thereby not taken into account, but could interact and redirect the upflow (Fontaine et al. 2014).

Compressional events have been observed in a similar setting south of LS volcano by Kong et al. (1992). Beneath the central volcano of the studied bathymetric high at the MAR, reverse faulting swarm events with similar trending as the events at LS volcano are observed. Tensional crack formation due to cooling of a recent intrusion as a mechanism for the reverse faulting is proposed. This theory is however in contrast with the hydrothermal cooling induced stress field established in previous studies (Sohn et al. 2004, Wilcock et al. 2009).

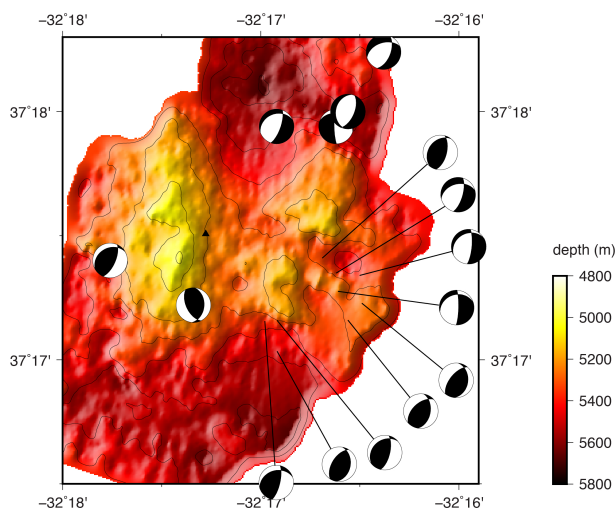


Figure 13 – Focal mechanisms plotted over a high resolution topographic map of the AMC roof (Combier et al. 2015). The size of the focal mechanisms does not correspond to the magnitude of the events.

spring 2009 fits this theory. At the end of march 2009, a $ML = 1.6$ compressional event is followed by two months of smaller events of normal faulting type ($ML \leq 0.5$). The model of static fatigue is inconsistent with the model proposed by Crawford et al. (2013) and Fontaine et al. (2014) and could lead to an alternative model for the hydrothermal cells.

The number of events considered in this study is too low to fully test or evaluate any theory on the hydrothermal circulation and state of stress at LS volcano. The seismicity to be triggered by a variety of complex processes of magnetic, tectonic and hydrothermal origin. A larger number of focal mechanisms over a longer time scale as well as of small magnitude events will improve the constraints on the actual stress distribution and its causes linked with the hydrothermal system. To further improve the model, seismicity could be associated with outflow fluid temperature which is influenced by cracking and collapse of the surrounding rocks (Sohn et al. 1999).

The focal mechanisms obtained in this study show a clear spatial pattern. Without taking the swarm events into account, normal faulting events on the northern peak and compressional events on the latitude of the southern peak can be observed. One possible mechanism for a compressional stress regime below the northern peak is static fatigue (Lister 1974), which describes the collapse of brittle material in the upwelling plume. With continuous microfracturing of the rock the cracks align vertically to form columns which collapse in compression. This collapse to fine material drastically reduces the permeability and changes the pore pressure of the surrounding rock. This would coincide with Johnson & McEvilly (1995), who link earthquake swarms along a fault plane to pore pressure changes. The apparent temporal pattern observed at the swarm activity in

6 Conclusion

P wave particle motion measurements on five seafloor seismometers around Lucky Strike volcano give consistent results on earthquake and whale song measurements to obtain an orientation angle for the horizontal components of the sensor. This allows better constrained focal mechanisms for microearthquakes ($-0.5 \leq ML \leq 1.8$) at LS volcano, by allowing the used amplitude ratios to obtain information on source mechanisms.

Events centred between the northern two peaks of the volcanic edifice indicate tensional stresses whereas compressional stresses dominate around the southern peak. A swarm activity after a big compressional event ($ML = 1.6$) shows normal faulting. Proposed models do not provide an explicit explanation for the stress distribution below Lucky Strike volcano.

Contradictory theories about the forces behind mid-ocean ridge volcano earthquakes highlight the complexity and non triviality of this problem. The microseismicity is most probably influenced by magmatic, hydrothermal and tectonic stresses, and long-term studies like that at LS could help to resolve between the different theories.

Further investigation on the available long-term data set and consideration of smaller events have to be conducted to get a better constraint on the state and evolution of stress at the Lucky Strike volcano.

7 Acknowledgements

This internship was made possible by the group of marine geosciences of the Institute de Physique du Globe de Paris. The support of the MIEM scholarship of Paris Diderot University allowed a trouble-free time in Paris. I would like to express my very great appreciation to my supervisor Dr. Wayne C. Crawford for his support, valuable advice and untiring patience. My grateful thanks are also extended to the scientific party on the PILAB cruise, especially Dr. Michael Kendall, Dr. Matthew R Agius and Dr. Saikiran Tharimena for their helpfulness in all scientific questions and making the cruise an unforgettable experience. I also would like to thank Dr. Javier Escartin, Dr. Mathilde Cannat and Caroline Gini for fruitful discussion on the geology and mechanisms defining Lucky Strike volcano. Furthermore I would like to express my gratitude to Prof. Heiner Igel and Dr. Joachim Wassermann for the support throughout my short scientific career. Finally, I wish to thank my family for their unconditional encouragement throughout my study.

References

- Aki, K. & Richards, P. G. (2002), *Quantitative seismology*, Vol. 1.
- Bani-Hassan, N., Iyer, K., Rüpké, L. H. & Borgia, A. (2012), 'Controls of bathymetric relief on hydrothermal fluid flow at mid-ocean ridges', *Geochemistry, Geophysics, Geosystems* **13**(5).
- Barreyre, T., Escartín, J., Garcia, R., Cannat, M., Mittelstaedt, E. & Prados, R. (2012), 'Structure, temporal evolution, and heat flux estimates from the lucky strike deep-sea hydrothermal field derived from seafloor image mosaics', *Geochemistry, Geophysics, Geosystems* **13**(4).
- Barruol, G., Reymond, D., Fontaine, F. R., Hyvernaud, O., Maurer, V. & Maamaatuiaahutapu, K. (2006), 'Characterizing swells in the southern pacific from seismic and infrasonic noise analyses', *Geophysical Journal International* **164**(3), 516–542.
- Blackman, D. K. & Kendall, J.-M. (1997), 'Sensitivity of teleseismic body waves to mineral texture and melt in the mantle beneath a mid-ocean ridge', *Philosophical Transactions of the Royal Society of London A: Mathematical, Physical and Engineering Sciences* **355**(1723), 217–231.
- Brown, R. J., Stewart, R. R., Gaiser, J. E. & Lawton, D. C. (2000), An acquisition polarity standard for multicomponent seismic data, Technical report, CREWES Research Report.
- Browning, J., Meredith, P. & Gudmundsson, A. (2016), 'Cooling-dominated cracking in thermally stressed volcanic rocks', *Geophysical Research Letters* **43**(16), 8417–8425.
- Cannat, M., Briais, A., Deplus, C., Escartin, J., Georgen, J., Lin, J., Mercouriev, S., Meyzen, C., Muller, M., Pouliquen, G. et al. (1999), 'Mid-atlantic ridge–azores hotspot interactions: along-axis migration of a hotspot-derived event of enhanced magmatism 10 to 4 ma ago', *Earth and Planetary Science Letters* **173**(3), 257–269.
- Colaco, A., Blandin, J., Cannat, M., Carval, T., Chavagnac, V., Connelly, D., Fabian, M., Ghiron, S., Goslin, J., Miranda, J. et al. (2011), 'Momar-d: a technological challenge to monitor the dynamics of the lucky strike vent ecosystem', *ICES Journal of Marine Science: Journal du Conseil* **68**(2), 416–424.
- Combier, V., Seher, T., Singh, S. C., Crawford, W. C., Cannat, M., Escartín, J. & Dusunur, D. (2015), 'Three-dimensional geometry of axial magma chamber roof and faults at lucky strike volcano on the mid-atlantic ridge', *Journal of Geophysical Research: Solid Earth* **120**(8), 5379–5400.
- Coutant, O. (1989), 'Program of numerical simulation axitra', *Res. Rep. LGIT (in French)*, Université Joseph Fourier, Grenoble .
- Crampin, S., Stephen, R. A. & McGonigle, R. (1982), 'The polarization of p-waves in anisotropic media', *Geophysical Journal International* **68**(2), 477–485.
- Crawford, W. C., Rai, A., Singh, S. C., Cannat, M., Escartin, J., Wang, H., Daniel, R. & Combier, V. (2013), 'Hydrothermal seismicity beneath the summit of lucky strike volcano, mid-atlantic ridge', *Earth and Planetary Science Letters* **373**, 118–128.
- Cuvelier, D., Sarrazin, J., Colaço, A., Copley, J., Desbruyères, D., Glover, A. G., Tyler, P. & Santos, R. S. (2009), 'Distribution and spatial variation of hydrothermal faunal assemblages at lucky strike (mid-atlantic ridge) revealed by high-resolution video image analysis', *Deep Sea Research Part I: Oceanographic Research Papers* **56**(11), 2026–2040.
- Dias, A., Mills, R., Taylor, R., Ferreira, P. & Barriga, F. (2008), 'Geochemistry of a sediment push-core from the lucky strike hydrothermal field, mid-atlantic ridge', *Chemical Geology* **247**(3), 339–351.

- Escartín, J., Barreyre, T., Cannat, M., Garcia, R., Gracias, N., Deschamps, A., Salocchi, A., Sarradin, P.-M. & Ballu, V. (2015), 'Hydrothermal activity along the slow-spreading lucky strike ridge segment (mid-atlantic ridge): Distribution, heatflux, and geological controls', *Earth and Planetary Science Letters* **431**, 173–185.
- Fontaine, F. J., Cannat, M., Escartin, J. & Crawford, W. C. (2014), 'Along-axis hydrothermal flow at the axis of slow spreading mid-ocean ridges: Insights from numerical models of the lucky strike vent field (mar)', *Geochemistry, Geophysics, Geosystems* **15**(7), 2918–2931.
- Fontaine, F. R., Barruol, G., Kennett, B. L., Bokelmann, G. H. & Reymond, D. (2009), 'Upper mantle anisotropy beneath australia and tahiti from p wave polarization: Implications for real-time earthquake location', *Journal of Geophysical Research: Solid Earth* **114**(B3).
- Gripp, A. E. & Gordon, R. G. (1990), 'Current plate velocities relative to the hotspots incorporating the nuel-1 global plate motion model', *Geophysical Research Letters* **17**(8), 1109–1112.
- Hardebeck, J. L. & Shearer, P. M. (2002), 'A new method for determining first-motion focal mechanisms', *Bulletin of the Seismological Society of America* **92**(6), 2264–2276.
- Hardebeck, J. L. & Shearer, P. M. (2003), 'Using s/p amplitude ratios to constrain the focal mechanisms of small earthquakes', *Bulletin of the Seismological Society of America* **93**(6), 2434–2444.
- Havskov, J. & Ottemöller, L. (2008), 'Seisan: The earthquake analysis software', *For Windows, Solaris, Linux and MACOSX. Version 8*.
- Hess, H. (1964), 'Seismic anisotropy of the uppermost mantle under oceans', *Nature* **203**(4945), 629–631.
- Humphris, S. E., Fornari, D. J., Scheirer, D. S., German, C. R. & Parson, L. M. (2002), 'Geotectonic setting of hydrothermal activity on the summit of lucky strike seamount (37°17'N, mid-atlantic ridge)', *Geochemistry, Geophysics, Geosystems* **3**(8), 1–25.
- Johnson, P. & McEvilly, T. (1995), 'Parkfield seismicity: Fluid-driven?', *Journal of Geophysical Research: Solid Earth* **100**(B7), 12937–12950.
- Jost, M. u. & Herrmann, R. (1989), 'A students guide to and review of moment tensors', *Seismological Research Letters* **60**(2), 37–57.
- Kisslinger, C. (1980), 'Evaluation of s to p amplitude ratios for determining focal mechanisms from regional network observations', *Bulletin of the Seismological Society of America* **70**(4), 999–1014.
- Kong, L. S., Solomon, S. C. & Purdy, G. (1992), 'Microearthquake characteristics of a mid-ocean ridge along-axis high', *Journal of Geophysical Research: Solid Earth* **97**(B2), 1659–1685.
- Krischer, L., Megies, T., Barsch, R., Beyreuther, M., Lecocq, T., Caudron, C. & Wassermann, J. (2015), 'Obspy: A bridge for seismology into the scientific python ecosystem', *Computational Science & Discovery* **8**(1), 014003.
- Lister, C. (1974), 'On the penetration of water into hot rock', *Geophysical Journal International* **39**(3), 465–509.
- Lowell, R. P. & Germanovich, L. N. (1994), 'On the temporal evolution of high-temperature hydrothermal systems at ocean ridge crests', *Journal of Geophysical Research: Solid Earth* **99**(B1), 565–575.

- Martins, I., Cosson, R. P., Riou, V., Sarradin, P.-M., Sarrazin, J., Santos, R. S. & Colaço, A. (2011), 'Relationship between metal levels in the vent mussel bathymodiolus azoricus and local microhabitat chemical characteristics of eiffel tower (lucky strike)', *Deep Sea Research Part I: Oceanographic Research Papers* **58**(3), 306–315.
- Nowacki, A. (2013), Mantle anisotropy beneath the earths mid-ocean ridges, in 'Plate Deformation from Cradle to Grave', Springer, pp. 61–97.
- Ondréas, H., Fouquet, Y., Voisset, M. & Radford-Knoery, J. (1997), 'Detailed study of three contiguous segments of the mid-atlantic ridge, south of the azores (37° n to 38° 30' n), using acoustic imaging coupled with submersible observations', *Marine Geophysical Research* **19**(3), 231–255.
- Scholz, J.-R., Barruol, G., Fontaine, F. R., Sigloch, K., Crawford, W. C. & Deen, M. (2017), 'Orienting ocean-bottom seismometers from p-wave and rayleigh wave polarizations', *Geophysical Journal International* **208**(3), 1277–1289.
- Schulte-Pelkum, V., Masters, G. & Shearer, P. M. (2001), 'Upper mantle anisotropy from long-period p polarization', *Journal of Geophysical Research: Solid Earth* **106**(B10), 21917–21934.
- Shearer, P. M. (2009), *Introduction to seismology*, Cambridge University Press.
- Singh, S. C., Crawford, W. C., Carton, H., Seher, T., Combier, V., Cannat, M., Canales, J. P., Düsünür, D., Escartin, J. & Miranda, J. M. (2006), 'Discovery of a magma chamber and faults beneath a mid-atlantic ridge hydrothermal field', *Nature* **442**(7106), 1029–1032.
- Snoke, J. A. (2003), 'Focmec: focal mechanism determinations', *International Handbook of Earthquake and Engineering Seismology* **85**, 1629–1630.
- Sohn, R. A., Barclay, A. H. & Webb, S. C. (2004), 'Microearthquake patterns following the 1998 eruption of axial volcano, juan de fuca ridge: Mechanical relaxation and thermal strain', *Journal of Geophysical Research: Solid Earth* **109**(B1).
- Sohn, R. A., Hildebrand, J. A. & Webb, S. C. (1999), 'A microearthquake survey of the high-temperature vent fields on the volcanically active east pacific rise (9° 50' n)', *Journal of Geophysical Research: Solid Earth* **104**(B11), 25367–25377.
- Thurnherr, A., Reverdin, G., Bouruet-Aubertot, P., St Laurent, L., Vangriesheim, A. & Ballu, V. (2008), 'Hydrography and flow in the lucky strike segment of the mid-atlantic ridge', *Journal of marine research* **66**(3), 347–372.
- Wilcock, W. S., Archer, S. D. & Purdy, G. (2002), 'Microearthquakes on the endeavour segment of the juan de fuca ridge', *Journal of Geophysical Research: Solid Earth* **107**(B12).
- Wilcock, W. S., Hooft, E. E., Toomey, D. R., McGill, P. R., Barclay, A. H., Stakes, D. S. & Ramirez, T. M. (2009), 'The role of magma injection in localizing black-smoker activity', *Nature Geoscience* **2**(7), 509–513.
- Zha, Y., Webb, S. C. & Menke, W. (2013), 'Determining the orientations of ocean bottom seismometers using ambient noise correlation', *Geophysical Research Letters* **40**(14), 3585–3590.

A Considerations for OBS orientation

When orienting OBSs, several factors should be taken into account before starting the analysis phase. These are presented below:

Instrumentation The first thing that needs to be checked is the outer circumstances to decide on which method to use to measure the orientation angle. Deployments of broadband instruments make it possible to make use of teleseismic waves and therefore P wave particle motion measurements as well as Rayleigh wave measurements (Scholz et al. 2017). Even though teleseismic events can be found in the recordings of short period instruments (geophones) it is very hard to pick reliable first arrivals. Therefore it is more advisable to study local and regional events if the instrument is a geophone. Another important aspect is the design of the instruments. Geophones traditionally have a right handed wiring, meaning the Z component is positive downward. Seismometers are wired after a left handed coordinate system, with Z being positive upward. This has to be taken into account when computing the incidence angle of the event.

Events Knowledge of errors on earthquake locations is important to not compare the measured BAZ to an expected BAZ with a high uncertainty. This strongly influences orientation angle measurements and the spread of the orientations for each station. Locations with large error ellipses have to be excluded from the measurements. If possible it is also advisable to use events with a flat incidence angle. Horizontal particle motions will then be more pronounced and measurements more reliable.

Measurement When performing the measurement it is important to start with some testings on the frequency band which will be used and also the window length for the analysis of the particle motion. In this study the start of the analysis window was set to the P wave arrival. Scholz et al. (2017) propose for low frequency recordings a window that starts several seconds before the P wave arrival. The different parameters have to be tested and adapted according to the data set. For the LS volcano a frequency band from 6 - 12 Hz was used and a window length of 0.3 s.

Orientation calculation Before orientation calculations, P wave particle motion measurements should be checked visually. Event recordings with a low SNR should be excluded, as strong noise can influence particle motions and therefore distort correct measurements. To ensure that only reliable measurements are taken into account thresholds for rectilinearity, measurement error and SNR of the data should be set.

